LAWRENCE
LIVERMORE
NATIONAL
LABORATORY

UCRL-CONF-208172

# Laser coupling to reduced-scale targets at the Early Light Program of the National Ignition Facility

D. E. Hinkel, M. B. Schneider, H. A. Baldis, D. Bower, K. M. Campbell, J. R. Celeste, S. Compton, R. Costa, E. L. Dewald, S.N. Dixit, M. J. Eckart, D. C. Eder, M. J. Edwards, A. Ellis, J. Emig, D. H. Froula, S. H. Glenzer, D. Hargrove, C. A. Haynam, R. F. Heeter, J. P. Holder, G. Holtmeier, L. James, K. S. Jancaitis, D. H. Kalantar, R. L. Kauffman, J. Kimbrough, R. K. Kirkwood, A. E. Koniges, J. Kamperschroer, O. L. Landen, M. Landon, A. B. Langdon, F. D. Lee, B. J. MacGowan, A. J. MacKinnon, K. R. Manes, M. J. May, J. W. McDonald, D. H. Munro, J. R. Murray, C. Niemann, D. Pellinen, V. Rekow, J. A. Ruppe, J. Schein, R. Shepherd, M. S. Singh, P. T. Springer, C. H. Still, L. J. Suter, R. E. Turner, R. J. Wallace, A. Warrick, P. Watts, F. Weber, E. A. Williams, B. K. Young, P. E. Young

November 29, 2004

46th Annual American Physical Society Division of Plasma Physics Meeting
Savannah, GA, United States
November 15, 2004 through November 19, 2004

## Disclaimer

# Laser coupling to reduced-scale targets at the Early Light Program of the National Ignition Facility

D. E. Hinkel, M. B. Schneider,

H. A. Baldis, D. Bower, K. M. Campbell, J. R. Celeste, S. Compton, R. Costa,

E. L. Dewald, S. N. Dixit, M. J. Eckart, D. C. Eder, M. J. Edwards, A. Ellis, J. Emig, D.

H. Froula, S. H. Glenzer, D. Hargrove, C. A. Haynam, R. F. Heeter,

J. P. Holder, G. Holtmeier, L. James, K. S. Jancaitis, D. H. Kalantar, R. L. Kauffman,

J. Kimbrough, R. K. Kirkwood, A. E. Koniges, J. Kamperschroer, O. L. Landen,

M. Landon, A. B. Langdon, F. D. Lee, B. J. MacGowan, A. J. MacKinnon,

K. R. Manes, M. J. May, J. W. McDonald, D. H. Munro, J. R. Murray,

C. Niemann, D. Pellinen, V. Rekow, J. A. Ruppe, J. Schein, R. Shepherd,

M. S. Singh, P. T. Springer, C. H. Still, L. J. Suter, R. E. Turner, R. J. Wallace,

A. Warrick, P. Watts, F. Weber, E. A. Williams, B. K. Young, P. E. Young

*University of California Lawrence Livermore National Laboratory*

*P. O. Box 808*

*Livermore, California 94550*

*hinkel1@llnl.gov*

# Abstract

A platform for analysis of material properties under extreme conditions, where a sample is bathed in radiation with a high temperature, is under development. This hot environment is produced with a laser by depositing maximum energy into a small, high-Z can. Such targets were recently included in an experimental campaign using the first four of the 192 beams of the National Ignition Facility, under construction at the University of California Lawrence Livermore National Laboratory. These targets demonstrate good laser coupling, reaching a radiation temperature of 340 eV. In addition, there is a unique wavelength dependence of the Raman backscattered light that is consistent with Brillouin backscatter of Raman forward scatter [A. B. Langdon and D. E. Hinkel, *Physical Review Letters* **89**, 015003 (2002)]. Finally, novel diagnostic capabilities indicate that 20% of the direct backscatter from these reduced-scale targets is in the polarization orthogonal to that of the incident light.



PACS numbers: 01.52+r, 52.25.Os, 52.35.Fp, 52.35.Mw, 52.38.Dx, 52.38.Hb, 52.38.Ph, 52.70.La

# I. INTRODUCTION

The advent of high-energy, high-power lasers such as the National Ignition Facility (NIF)[1] at the University of California Lawrence Livermore National Laboratory (LLNL) and the Laser MegaJoule (LMJ)[2] in France provides access to a new and exciting regime of high energy density science. Experiments to occur on these facilities range from inertial confinement fusion[3] to the study of material properties under extreme conditions. To examine material properties at extreme temperatures, an appropriate platform must be developed and analyzed, where a sample is bathed in radiation of a known temperature. It is the creation of such an environment that we address here.

We produce a hot environment by depositing all available laser energy into the smallest, high-Z enclosure possible (c.f. Fig. 1). Material in the can wall is excited, ionized, and heated by the laser. Most of the absorbed energy is re-radiated, filling the can with x-radiation.

Depositing maximum laser energy into a small can causes the target to fill with ablated wall material on the time scale of the laser pulse. The ablated material then absorbs laser energy before it reaches the wall, limiting energy deposition. Further, the laser spot size is constrained to be smaller than the can opening, so small cans result in high laser intensities. Target filling at high laser intensities accesses a new region of parameter space where we must mitigate laser-plasma interactions (LPI).

Hot environments have been generated at the Omega laser, located at the University of Rochester's Laboratory for Laser Energetics. Most recently, these targets

were used during an experimental campaign on NIF Early Light (NEL), the first four beams of the full NIF configuration. Such experiments are crucial to the understanding of laser-target coupling in small targets.

We investigated laser-target coupling on NEL with two different sizes of gold cans. The first can has a 560 μm diameter and is 525 μm in length, whereas the second has a diameter of 600 μm and is 660 μm in length. The aspect ratio of the second was purposefully chosen to be different from that of the first. The smaller of these cans will fill more quickly with ablated gold plasma, which then flows outward through the entrance hole. The plasma outside the target will be at a higher density in the smaller can, and since self-focusing and filamentation[5] of the laser light scale with plasma electron density, it will be more vigorous for this target. [Filamentation occurs when the laser interacts with density perturbations, ponderomotively creating density depressions into which the beam then refracts, further driving the density depression]

In both targets, filamentation can cause the beam to spray into an angle so large that the beam spot size becomes greater than the can diameter at its entrance hole. However, not only does the larger target have a relatively longer length, thereby more readily accommodating plasma fill, but it also has a larger diameter. Thus it can also accommodate a larger angle of beam spray. We therefore hypothesize that this target will show a greater degree of laser-target coupling.

Another mechanism that reduces coupling is laser scatter. Backscatter of the laser light occurs via different mechanisms[6]. In Brillouin backscatter (SBS), the incident laser light scatters off ion acoustic waves, propagating in the same direction, into a backward-propagating light wave. Raman backscatter (SRS) occurs when the incident

laser light scatters off electron plasma waves into backward-propagating light. Such mechanisms represent a direct loss of energy that would otherwise go toward heating the can.

Another means of laser scatter also reduces coupling. Laser light can undergo Raman forward scatter (RFS), where incident laser light scatters off a co-propagating electron plasma wave into a forward light wave. Raman forward scatter may not reduce coupling, as the light is still propagating in the same direction as before the scatter process, albeit at a shifted frequency and wavenumber. However, in these targets, where the electron temperature is high (> 7 keV) as well as the plasma density, the Raman forward scattered light is itself intense enough to undergo backscatter[7], a process we call Raman re-scatter.

We present here results from and analysis of our recent experimental campaign at NIF Early Light. Reduced-scale cans shot at NEL demonstrate good laser-target coupling, where the flux of radiation (as measured by Dante[8], an absolutely calibrated x-ray spectrometer) escaping the targets exceeded 1000 GW/sr. In fact, the 560-μm-diameter target reached a radiation temperature of 340 eV, and the 600-μm-diameter target reached 337 eV.

The collected backscatter was typically 15%, and was predominantly SBS (> 11%). This measurement includes the backscatter directly back into the lens, collected by the Full Aperture Backscatter Station (FABS)[9], as well as that to a scatter plate surrounding the beam ports, the Near-Backscatter Imager (NBI)[10]. The backscatter to the FABS is spectrally analyzed. We find that the SBS collected by the FABS exhibits a temporal dependence that does not interfere with the peak radiation drive, occurring in

one burst in the first half of our 1.1 ns pulse, and in a second burst before the time of peak radiation drive. Such behavior in the SBS has been accounted for in radiation-hydrodynamics simulations performed using Lasnex[11].

The Raman backscatter collected by the FABS shows a unique wavelength dependence when the beams are fully conditioned. When the beams are smoothed both with partial-spatial and with polarization smoothing, SRS occurs at two distinct wavelengths throughout the entire pulse, whereas when they are only partially spatially smoothed, the SRS spectrum shows evidence of filamentation. This is consistent with Raman re-scatter as described above.

Light collected on the NBI is backscatter from those portions of the beam that have filamented and sprayed. Over 70% of the backscatter collected was on the NBI plate, strong evidence that filamentation of laser light occurs in these targets.

One of our most interesting findings relies on the unique diagnostic capabilities at NEL. When the incident laser beam is linearly polarized in one polarization, 20% of the backscatter is found to be in the orthogonal polarization. Mechanisms that might cause such a de-polarization are being investigated.

This paper is organized as follows. In Sec. II, we describe the NIF laser, its capabilities, and the Early Light Program. In Sec. III we present our radiation drive results and analyses. Sec. IV details the LPI measurements and comparisons to simulations. Our findings are summarized in the Conclusion, Sec. V.

## II. NIF EARLY LIGHT

The NIF laser, upon completion, will be comprised of 192 beams with *f*-number 20 that undergo amplification at a wavelength $\lambda_0 = 1.053$ μm. Quads of 4 closely-spaced beams overlap at the target, providing 48 *f*/8 incident beams. Frequency conversion is to the third harmonic, i.e., 3ω (351 nm). The laser is designed to deliver a maximum energy of 1.8 MJ and provide a peak power of 700 TW.

The first quad of NIF has been commissioned to target chamber center, as depicted in Fig. 2. This quad of beams enters the target chamber at the bottom left, where the FABS is located. The Dante x-ray spectrometer is below the equator, viewing the laser entrance hole of the target at a $21^0$ angle. The NBI is located across the target chamber from the laser beam ports, where cameras take pictures of the scatter plate around the ports. Many other diagnostics (c.f. Fig. 2) were utilized during these experiments, but are beyond the scope of this paper. The diagnostics of Fig. 2 have been commissioned for use at NIF, and, along with the first quad of laser beams, comprise NEL.

Our targets were oriented so that the beam quad propagates along the target axis, hitting the back wall. In this geometry we expect little beam deflection[12] caused by transverse plasma flow. Further, crossed-beam energy transfer[13] occurs between beams within the quad, and thus does not reduce coupling. NEL provides the opportunity to de-couple filamentation from these above-mentioned processes, and to assess its impact alone on laser-target coupling.

Since both laser scatter and spray have gain rates that scale with intensity, we

attempt to mitigate these coupling losses by reducing the amount of laser power at high intensities in the beam. Fig. 3a is a plot of a NIF laser beam at best focus. The spot size is roughly 250 μm in diameter, and has 10% of its power in intensities greater than 6.9 x $10^{16}$ W/cm$^2$ when the input quad contains 8.5 TW.

Phase plates are typically used to spatially smooth the beam, resulting in a 500 μm spot size in other NEL experiments. For the reduced-scale targets used in these experiments, such a spot size is too large and would result in reduced laser coupling as the target heats up and fills with plasma. We therefore utilize beams that are partially smoothed spatially using small-spot phase plates[14], as depicted in Fig. 3b. These phase plates distribute the laser power into a slightly larger, speckled beam that results in a spot approximately 300 μm in diameter. This spot contains greater than 90% of the energy, and has 10% of its power in intensities greater than 3.8 x $10^{16}$ W/cm$^2$.

We further condition the beam with polarization smoothing[15]. Here, the laser light is split into two orthogonal polarizations, and these intensity patterns are displaced by 30 μm. This results in a further reduction in power in intense speckles, so that 10% of the power is in intensities greater than 2.65 x $10^{16}$ W/cm$^2$, as shown in Fig. 3c.

We discuss here five shots with reduced-scale targets. All the shots used a 1.1nS square pulse and the small-spot phase plates. The first three shots also used the polarization smoothing crystals. Shot One, heretofore referred to as the low energy shot, had 6.12 kJ entering the 560 μm target. Shot Two was also into the 560 μm target, but at a higher energy of 9.46 kJ. Shot Three was also at high energy (9.2 kJ) but into a 600 μm diameter can. Finally, Shots Four and Five were a repeat of Shots Two and Three at energies of 9.75 and 9.43 kJ, respectively, but without the polarization smoothing

crystals.

From this matrix of shots, we assess the energy coupling by measuring the radiation drive and analyzing the laser scatter and spray, topics of the next two sections.

## III. RADIATION DRIVE

Reduced scale targets are sufficiently different from targets in the ignition regime that it is worthwhile to note these differences, summarized in Fig. 4. Both targets will ultimately indirectly drive (by conversion of laser to x-ray conversion in a high-Z container) either an ignition capsule or a materials science sample, but do so under different conditions. In the ignition target, LPI primarily occurs inside the target rather than outside, as in the reduced-scale target. This is because ignition targets are larger, and thus do not fill to the extent that the smaller targets do. For this same reason, LPI occurs at a higher density ($n_e/n_c < 0.4$ as opposed to $n_e/n_c < 0.15$) in reduced scale targets. LPI also occurs at higher electron temperature ($T_e < 50$ keV as opposed to $T_e < 5$ keV) because laser energy is deposited within a smaller volume in the reduced-scale targets.

Filamentation is deleterious to both targets, but for different reasons. In an ignition target, filamentation can impact the symmetry of an ignition capsule during implosion, as it alters the laser spot configuration on the walls. In reduced-scale targets, filamentation results in reduced energy coupling if the beams spray into a spot size too large to enter the high-Z can Laser scatter also represents an energy coupling loss for both targets. Finally, hot electrons produced from LPI can pre-heat the capsule/sample in both types of targets.

In reduced-scale targets, more is demanded in terms of laser performance. High

energy in a short pulse is required, and, since the targets are small, the spot size is smaller than for an ignition target. Typically the spot size is less than 400 μm in these targets, whereas in an ignition target spot sizes are usually 700 μm, or larger

More power in a smaller spot means that reduced-scale targets are driven at higher intensity. In this regime of high laser intensity, electron density and electron temperature, it is important to learn how reduced-scale targets perform as their size is decreased. Such an investigation provides information on optimizing target size as a function of laser performance, and supplies scientific understanding of this relatively unexplored parameter regime.

We analyze target performance in these reduced-scale targets by measuring the thermal radiation flux emitted from the laser entrance hole (LEH). The flux is measured with Dante, an absolutely calibrated, time-resolved x-ray spectrometer. Three mirror-filter and seven filter channels collect x-rays with energies between 50 eV and 1.8 keV, and eight filter channels collect x-rays with energies between 1.8 and 9.5 keV. Absolutely calibrated x-ray diodes measure the flux intensity in each channel, and a radiation temperature, Tr is derived:

$$T_r = \{\pi P_{Dante}/[\sigma A_{LEH} \cos(21^0)]\}^{1/4}, \quad (1)$$

where $T_r$ is the radiation temperature, $P_{Dante}$ is the measured radiation flux (power/solid angle), $\sigma$ is the Stefan-Boltzmann constant, and $A_{LEH}$ is the area of the laser entrance hole through which the radiation leaves the target.

Figs. 5 summarize the Dante results, where measured radiation flux versus time is presented, and compared to the Lasnex simulations which account for 10% backscatter with a temporal profile similar to that of SBS, i.e., peaking before 500 ps and again

before 1100 ps. Fig. 5a shows the GW/sr measured in Shot One as a function of time. This low-energy shot demonstrates excellent energy coupling, resulting in nearly 800 GW/sr of measured radiation flux, or a radiation temperature $T_r$ = 318 eV. Surprisingly, Lasnex simulations calculate a lower level of flux than is measured in experiment, $T_r$ (LASNEX) = 307 eV.

In Fig. 5b we present the measured radiation flux versus time for the 560 μm-diameter target at high energy with polarization smoothing (Shot Two) and without polarization smoothing (Shot Four). Shot Two achieved a radiation temperature of 340 eV, similar to the Lasnex prediction. Shot Four at slightly higher energy resulted in $T_r$ = 337 eV, whereas Lasnex predicted 343 eV. The lack of polarization smoothing on Shot Four decreased the coupling by ~ 8% in this target. [The energy coupling as defined here is the output radiation flux / input laser energy.]

The energy coupling at high energy even with polarization smoothing is only 80% of that in the low energy shot. This suggests that even with polarization smoothing, beam spray is limiting coupling, as the fractional backscatter in the low energy shot is nearly identical to that of the high energy shot

Fig. 5c summarizes the radiation drive results for the 600 μm-diameter target with polarization smoothing (Shot Three) and without polarization smoothing (Shot Five). Here, the measured flux without polarization smoothing is 25% lower than with polarization smoothing, resulting in radiation temperatures of 337 and 315 eV, respectively. Lasnex simulations of these shots demonstrate radiation temperatures of 320 and 322 eV, respectively.

Even though Shot One takes place at low energy, the target nonetheless fills with

ablated gold plasma during the laser pulse. Here, our simulation underpredicts the radiation flux out of the can. We conjecture that Lasnex may be overestimating target fill, which would result in a lower radiation flux as seen by Dante. Also, in these simulations, we have not accounted for hot electrons generated by Raman scatter. Re-fluxing of hot electrons through the walls could increase the radiation inside the target as well.

For both Shots Two and Four, simulations show agreement with experimental results. This is consistent with Lasnex overpredicting target fill, thereby reducing the radiation flux. A back-of-the envelope calculation (which does not account for hydrodynamics motion) predicts that these targets could attain a radiation temperature as high as $T_r \sim 358$ eV.

Finally, when we compare the radiation flux measurements of Shots Three and Five, Lasnex does not agree with Shot Three, which had a greater flux, but with Shot Five, which showed a marked reduction in radiation drive without polarization smoothing. Such a scenario would again be consistent with too much filling, or with not accounting for such processes as hot electron re-flux through the walls.

In previous campaigns at the Omega laser, Lasnex has consistently overpredicted the radiation drive in reduced-scale targets.[16] In these experiments, coupling is further decremented by beam deflection and crossed-beam energy transfer outside of the target. These NEL shots provide unique insight and guidance for our radiation-hydrodynamics simulations, and this information will enhance our computational capability.

## IV. LASER SCATTER

Laser backscatter losses reduce target coupling, resulting in a cooler environment. Analysis of such processes serves to increase our understanding of LPI with the ultimate goal of mitigation. For these stimulated interactions, both frequency and wavenumber matching must occur, i.e., $\omega_{inc} = \omega_{ref} + \omega_{iaw,epw}$, $k_{inc} = k_{ref} + k_{iaw,epw}$. Here, $[(\omega_{inc},k_{inc}), (\omega_{ref},k_{ref}), (\omega_{iaw},k_{iaw}), (\omega_{epw}, k_{epw})]$ are the frequency and wavenumber of the incident, reflected, ion acoustic and electron plasma waves, respectively.

The backscatter for these experiments was about 16%, and was dominated by SBS on the NBI plate, which accounts for 70% of the total backscatter. Approximately 1% of the total backscatter was SRS on the NBI plate. The presence of 71% of the backscatter on the NBI corroborates the presence of filamentation in these experiments.

The direct-backscatter SBS, collected by FABS, was about 3%. SBS occurs early in the pulse, at about 250 ps, at a blue shift of 3Å, and then later in the pulse, around 700-800 ps with either no blue shift, or a slight red shift (with respect to the incident light).

SRS to the FABS is at approximately 1-2%. While the Raman levels are low, the spectrum contains information about the electron density and temperature at which scatter is occurring, which provides us with some information about the plasma characterization. Fig. 6a is a plot of the Raman backscatter for Shot One, the low energy shot. The spectrum peaks in wavelength at about 640 nm, and also in time at about 600 ps. This corresponds to an electron plasma density of $n_e = 0.14\ n_c$ (where $n_c = 9 \times 10^{21}$ $cm^{-3}$ is the critical density for light of wavelength 0.351 μm) and an electron temperature $T_e = 7$ keV.

At higher energy, as in Shot Two, the Raman spectrum changes, as depicted in Fig. 6b. Here SRS occurs throughout the entire pulse, and peaks at two wavelengths, 590 nm and 660 nm. This could be SRS occurring at two different places in the target, but late in time, SRS can only occur on a density gradient outside the target, which is not consistent with such a scenario. Another possible mechanism, that doesn't occur at low intensity such as in Shot One, but does at high intensity, is that the peak at 660 nm is Raman backscatter, but that at 590 nm is Brillouin backscatter of Raman forward scatter. Here the incident light forward scatters off electron plasma waves to such a degree that the forward scattered light itself is above threshold for Brillouin backscatter. (At this plasma density, frequency matching cannot occur for Raman backscatter.)

Another change in the spectrum occurs when polarization smoothing is removed, (as in Shot Four), shown in Fig. 6c. Here, the Raman spectrum peaks at lower density (shorter wavelength) as time increases. It is likely here that SRS, occurring on a density gradient outside the target, is getting pushed to lower density as the incident light filaments. Such changes in the spectra between shots with and without polarization smoothing are evidence that polarization smoothing is indeed suppressing filamentation.

In Fig. 6d, we plot results from a one-dimensional particle-in-cell simulation, performed with Zohar[17], at an intensity $I = 1 \times 10^{16}$ W/cm$^2$, an electron plasma density $n_e = 0.15\ n_c$, and an electron temperature $T_e = 7$ keV. In this simulation, SRS occurs at 650 nm, and SBS of Raman forward scatter at 580 nm. Thus, our interpretation of the spectrum is consistent with re-scatter of Raman forward scatter by SBS. If Thomson scatter could detect the presence of the ion acoustic wave associated with this process, which occurs at about $0.9\ k_{inc}$ for these parameters, then the presence of re-scatter would

be confirmed.

Another interesting feature of the backscatter data is that for both shots without polarization smoothing, 20% of the direct backscatter (collected by FABS) was de-polarized, i.e., was in the polarization orthogonal to that of the incident light. Faraday rotation could cause such a de-polarization, provided there is a magnetic field along the direction of propagation, i.e, $B_z$.

Hydrodynamic magnetic fields, such as those generated by $\nabla n \times \nabla T$ effects, will not be along the propagation direction, but rather in the angular direction, i.e., $B_\theta$. Micro-scale magnetic fields, such as those generated by hot electrons from Raman scatter in intense speckles[18] will also produce $B_\theta$.

We are investigating other mechanisms that could cause de-polarization of the backscatter. Multiple scatterings from turning points near critical surfaces within the target might be a candidate, but these targets fill with plasma quickly, and only reach the critical surface early in the laser pulse, i.e., within the first 200 ps. Later in time, the light is absorbed in underdense plasma well before its turning point. Since this particular data is not time resolved, we do not know whether this is a likely scenario.

## V. CONCLUSIONS

Analyses of experiments presented in this paper show that the reduced-scale targets shot on NIF Early Light have unique characteristics that further our understanding of laser-material interactions. These targets emit a radiation flux in excess of 1000 GW/sr, exhibit features in the Raman spectrum which are consistent with re-scatter of

Raman forward scatter, and show de-polarization in the backscatter of polarized incident light.

We used two different-sized targets, with different aspect ratios, to investigate the efficiency of laser light coupling to these targets. We found that the target with the slightly larger diameter (600 μm versus 560 μm) and longer length (660 μm versus 525 μm) showed a greater degree of coupling when polarization smoothing was used to further condition partially spatially smoothed beams. Radiation-hydrodynamics simulations with Lasnex under-predicted the radiation drive of this particular target with greater coupling. This may be a consequence of the target filling too rapidly in the simulations, or, perhaps it is an enhancement in coupling produced by hot electrons re-fluxing through the target walls, a physical process that was not included in the simulations reported here.

At high intensity, and when the beams were conditioned with both small-spot phase plates and polarization smoothing, the Raman spectrum is consistent with Raman re-scatter, where Raman forward-scattered light itself undergoes Brillouin backscatter. To date, re-scatter has only been identified in simulations. It is likely that the simplified, on-axis geometry of the high-energy NEL beams has provided a platform where such a mechanism is more readily analyzed. Experiments with Thomson scatter off the ion acoustic wave associated with re-scatter would absolutely ascertain the presence of re-scatter in indirectly-driven targets.

We are investigating mechanisms that de-polarize backscatter of polarized incident light. Lasnex simulations including magnetic fields are being performed, and PIC simulations are being re-visited. Such investigations serve to further our

understanding of laser-target interactions.

These were the last shots on NIF Early Light, as the facility closes down to begin construction on the next 44 beam lines, bringing up NIF First Cluster. Important diagnostics were commissioned on NIF Early Light, and interesting physics questions arose from the campaigns. Analysis of NEL experiments will help us prepare for future experiments on NIF first cluster, which hold the promise for even more exciting science.

This work was performed under the auspices of the U.S. Department of Energy by the University of California, Lawrence Livermore National Laboratory under Contract No. W-7405-Eng-48.

## References


[1]J. A. Paisner, E. M. Campbell, and W. J. Hogan, Fusion Technol. **26**, 755 (1994).

[2]M. L. Andre, "Status of the LMJ Project", Proc. SPIE Int. Soc. Opt. Eng. **3047**, 38 (1997).

[3]J. H. Nuckolls, L. Wood, A. Thiessen, and G. B. Zimmerman, Nature **239**, 139 (1972); J. D. Lindl, *Inertial Confinement Fusion* (Springer-Verlag, New York, 1998).

[4]E. Dattolo, L. Suter, M-C. Monteil *et al.*, Phys. Plasmas **8**, 260 (2001); D. E. Hinkel, M. B. Schneider, A. B. Langdon, and L. J. Suter, Bull. Am. Phys. Soc. **46**, 296 (2001).

[5]F. W. Perkins and E. J. Valeo, Phys. Rev. Lett. **32**, 1234 (1974); W. L. Kruer, Comments Plasma Phys. Control. Fusion **9**, 63 (1985); R. L. Berger, B. F. Lasinski, T. B. Kaiser, E. A. Williams, A. B. Langdon, and B. I. Cohen, Phys. Fluids B **5**, 2243 (1993); P. E. Young, M. E. Foord, J. H. Hammer, W. L. Kruer, M. Tabak, and S. C. Wilks, Phys. Rev. Lett. **75**, 1082 (1995).

[6]V. P. Silin, Sov. Phys. JETP **21**, 1127 (1965); J. F. Drake, P. K. Kaw, Y. C. Lee, G. Schmid, C. S. Liu, and M. N. Rosenbluth, Phys. Fluids **17**, 778 (1974); D. W. Forslund, J. M. Kindel, and E. L. Lindman, Phys. Fluids **18**, 1002 (1975); W. L. Kruer, *The Physics of Laser Plasma Interactions* , Frontiers in Physics Series Vol. 73 (Addison-Wesley, Redwood City, CA, 1988).

[7]A. B. Langdon and D. E. Hinkel. *Phys. Rev. Lett.* **89**, 015003 (2002).

[8]E. L. Dewald, K. M. Campbell, R. E. Turner *et al.*, Rev. Sci. Inst. **75**, 3759 (2004).

[9]D. H. Froula, D. Bower, M. Chrisp *et al.*, Rev. Sci. Inst. **75**, 4168 (2004); R. K. Kirkwood, T. McCarville, D. H. Froula *et al.*, Rev. Sci. Inst. **75**, 4174 (2004); D. E. Bower, T. J. McCarville, S. S. Alvarez *et al.*, Rev. Sci. Inst. **75**, 4177 (2004).

[10]A. J. Mackinnon, T. McCarville, K. Piston *et al.*, Rev. Sci, Inst. **75**, 4183 (2004).

[11]G. B. Zimmerman and W. L. Kruer, Comments Plasma Phys. Cont. Fusion **2**, 85 (1975).

[12]H. A. Rose (private communication, LLNL, 1995); J. D. Moody, B. J. MacGowan, D. E. Hinkel, W. L. Kruer, E. A. Williams, K. Estabrook, R. L. Berger, R. K. Kirkwood, D. S. Montgomery, and T. D. Shepard, Phys. Rev. Lett. **77**, 1294 (1996); D. E. Hinkel, E. A. Williams, and C. H. Still, Phys. Rev. Lett. **77**, 1298 (1996).

[13]R. K. Kirkwood, B. B. Afeyan, W. L. Kruer, B. J. MacGowan, J. D. Moody, D. S. Montgomery, D. M. Pennington, T. L. Weiland, and S. C. Wilks, Phys. Rev. Lett. **76**, 2065 (1996); W. L. Kruer, S. C. Wilks, B. B. Afeyan, and R. K. Kirkwood, Phys. Plasmas **3**, 382 (1996); E. A. Williams, B. I. Cohen, L. Divol, M. R. Dorr, J. A. Hittinger, D. E. Hinkel, A. B. Langdon, R. K. Kirkwood, D. H. Froula,, and S. H. Glenzer, Phys. Plasmas **11**, 231 (2004).

[14]J. A. Menapace, S. N. Dixit, F. Y. Genin, and W. F. Brocious, SPIE Proceedings of Damage Symposium, Boulder, CO, 2003.

[15]E. Lefebvre, R. L. Berger, A. B. Langdon, B. J. MacGowan, J. E. Rothenberg, and E. A. Williams, Phys. Plasmas **5**, 2701 (1998); T. R. Boehly, V. A. Smalyuk, D. D. Meyerhofer *et al.*, J. Appl. Phys. **85**, 3444 (1999); J. E. Rothenberg, *ibid.* **87**, 3654

(2000); D. H. Munro, S. N. Dixit, A. B. Langdon, and J. R. Murray, accepted, *Appl. Optics,* 2004.

[16]D. E. Hinkel, M. B. Schneider, E. A. Williams, A. B. Langdon, L. J. Suter, and P. T. Springer, Third International Conference on Inertial Fusion Sciences and Applications, 2003, edited by B. A. Hammel, D. D. Meyerhofer, J. Meyer-ter-Vehn, H. Azechi (American Nuclear Society, Inc., 2004) 242.

[17]A. B. Langdon and B. F. Lasinski, *Methods in Computational Physics* (Academic Press, New York, 1976), Vol. 16, pp. 327-366.

[18]B. F. Lasinski, C. H. Still, A. B. Langdon, D. E. Hinkel, and E. A. Williams, Third International Conference on Inertial Fusion Sciences and Applications, 2003, edited by B. A. Hammel, D. D. Meyerhofer, J. Meyer-ter-Vehn, H. Azechi (American Nuclear Society, Inc., 2004), p. 272.

## Figure Captions

**Fig. 1.** Experimental configuration at NIF Early Light (NEL) for reduced-scale targets. The first four of the 192 beams of full NIF enter the can centered on-axis. X-radiation leaving the can is collected at an angle of $21^0$, and burnthrough radiation is collected through the sides of the can at $84^0$ relative to the target axis. The direct backscatter is collected by FABS and spectrally analyzed. Near backscatter is collected by the NBI plate.

**Fig. 2.** Target chamber and diagnostics at NEL. The quad of beams enters the target chamber at the bottom left-hand side, where the FABS is located. The x-ray spectrometer, Dante, is located below the equator and views the laser entrance hole of the target at an angle of $21^0$. The NBI, across the chamber from where the beam lines enter, takes pictures of the scatter plate surrounding the beam ports.

**Fig. 3.** A plot of the NIF beam quad cross section at best focus: (a) the unsmoothed quad has a spot size of 250 μm, with 10% of the power in intensities greater than $6.9 \times 10^{16}$ W/cm$^2$; (b) the partially-spatially smoothed NIF beam quad, where small-spot phase plates are utilized. Partial spatial smoothing increases the spot size to 300 μm and reduces the power at high intensity. Here, the quad has 10% of the power in intensities greater than $3.8 \times 10^{16}$ W/cm$^2$; (c) the NIF beam quad, where both small-spot phase plates and polarization smoothing are used. Polarization smoothing, which nearly halves the power in intense laser speckles, further reduces the power at high intensity without

increasing the spot size. With polarization smoothing, the quad has 10% of its power in intensities greater than $2.65 \times 10^{16}$ W/cm$^2$.

**Fig. 4.** Laser-plasma interactions (LPI) affect ignition and reduced-scale targets differently. LPI takes place outside of a target at reduced scale, where the electron density and temperature are much higher than in an ignition target. LPI is deleterious to these targets for different reasons: in the ignition target, implosion symmetry and energy coupling losses occur, caused by filamentation and laser backscatter; in the reduced-scale target, filamentation and laser backscatter both represent a reduction in energy coupling to the target. Reduced-scale targets also demand more performance from the laser, requiring high energy in short laser pulses in small spots.

**Fig. 5.** Radiation flux versus time, for: (a) The 560 μm-diameter target shot at low energy (6.12 kJ) with polarization smoothing and small-spot phase plates (solid curve). The Lasnex simulation is denoted by the dashed curve. (b) The 560 μm-diameter target shot at high energy (9.46 kJ for #2 and 9.75 kJ for #4) with polarization smoothing (#2) and without (#4). The dashed curves represent the Lasnex results at the correct laser input energy. (c) The 600 μm-diameter target shot at high energy (9.2 kJ for #3 and 9.43 kJ for #5) with polarization smoothing (#3) and without (#5). Lasnex results are depicted by the dashed curves.

**Figs. 6.** Plots of the Raman spectrum for: (a) The 560 μm-diameter target shot at low energy (6.12 kJ) with polarization smoothing and small-spot phase plates. The SRS peak

is consistent with occurrence at an electron plasma density $n_e/n_c = 0.14$ and an electron temperature $T_e = 7$ keV. (b) The 560 μm-diameter target shot at high energy (9.46 kJ) with polarization smoothing and small-spot phase plates. The SRS shows a dependence on wavelength that is consistent with SBS of Raman forward scatter, where Raman backscatter occurs at 660 nm, and SBS of Raman forward scatter at 590 nm. (c) The 560 μm-diameter target shot at high energy without polarization smoothing, but with small-spot phase plates. The SRS spectrum peaks at lower density (shorter wavelength) as time increases, a scenario consistent with filamentation.

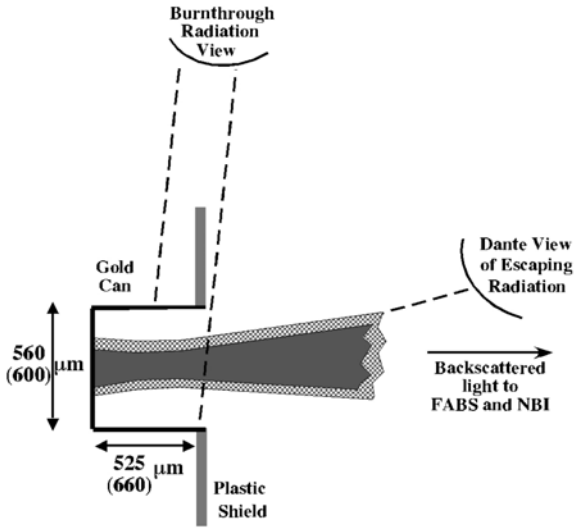
Burnthrough
Radiation
View
Gold
Can
Dante View
of Escaping
Radiation
560
(600) μm
Backscattered
light to
FABS and NBI
525 μm
(660)
Plastic
Shield

Fig. 1

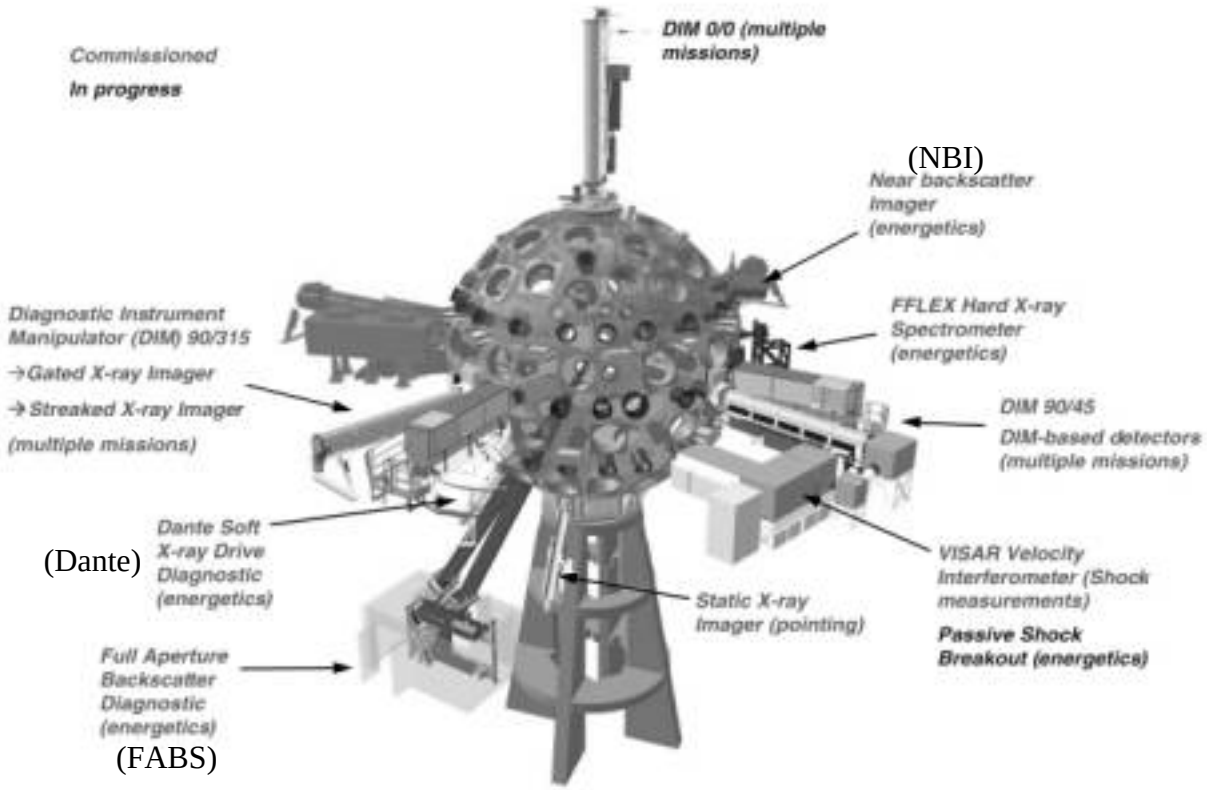
Commissioned
In progress
DIM 0/0 (multiple missions)
(NBI)
Near backscatter Imager (energetics)
FFLEX Hard X-ray Spectrometer (energetics)
Diagnostic Instrument Manipulator (DIM) 90/315
→Gated X-ray Imager
→ Streaked X-ray Imager
(multiple missions)
DIM 90/45
DIM-based detectors (multiple missions)
(Dante)
Dante Soft X-ray Drive Diagnostic (energetics)
VISAR Velocity Interferometer (Shock measurements)
Passive Shock Breakout (energetics)
Static X-ray Imager (pointing)
Full Aperture Backscatter Diagnostic (energetics)
(FABS)

Fig. 2

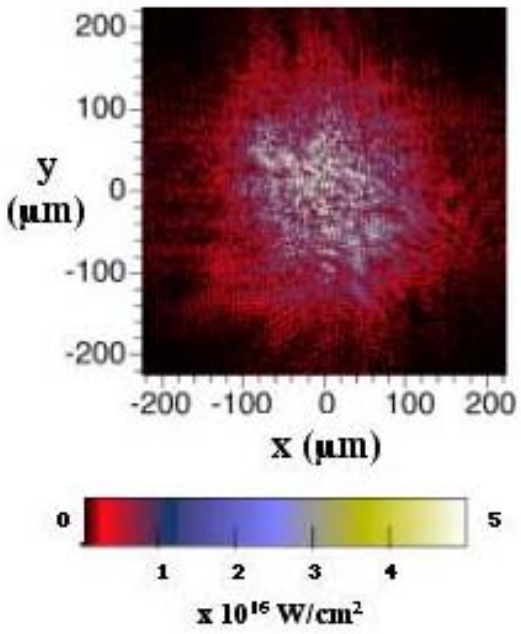


Fig. 3a

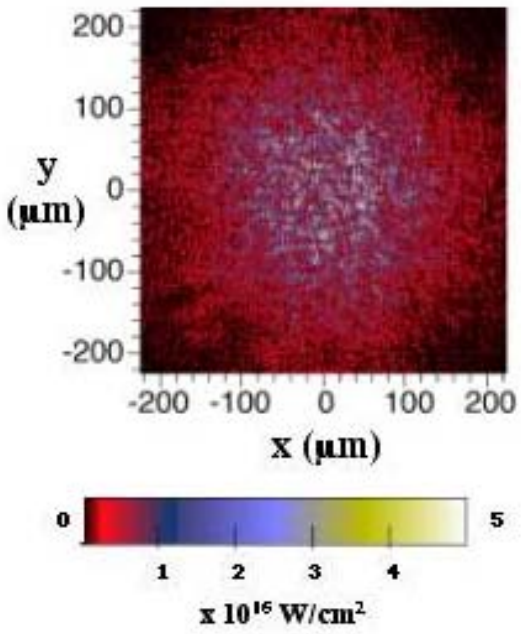


Fig. 3b

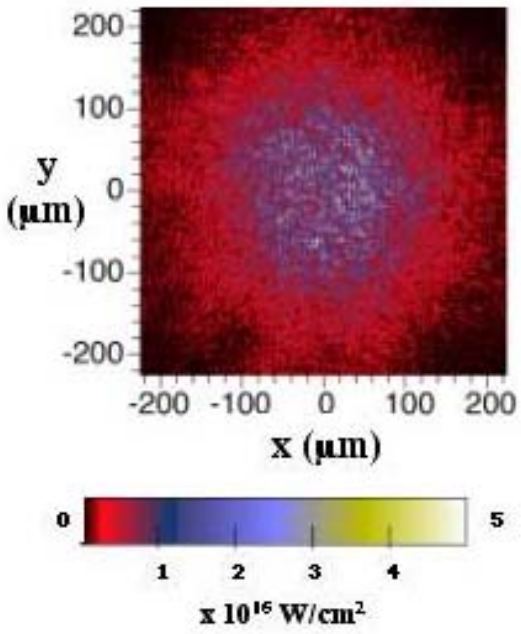


Fig. 3c

| Laser-Plasma Interaction (LPI) Issues | | |
|---|---|---|
| Hohlraum: | Ignition | HTH |
| Where? | Inside | Outside |
| $n_e/n_c$ | < 0.15 | < 0.4 |
| $T_e$ | 2-5 keV | < 50 keV |
| Filamentation/ deflection | Impacts symmetry | Reduces coupling |
| SRS, SBS | Reduce energy coupling | |
| Hot electrons | Pre-heat | |

| Laser Performance | | |
|---|---|---|
| Spot size, μm | 700, rms | < 400 |
| Intensity, $W/cm^2$ @ LEH | $2 \times 10^{15}$ | $> 1 \times 10^{16}$ |

Fig. 4

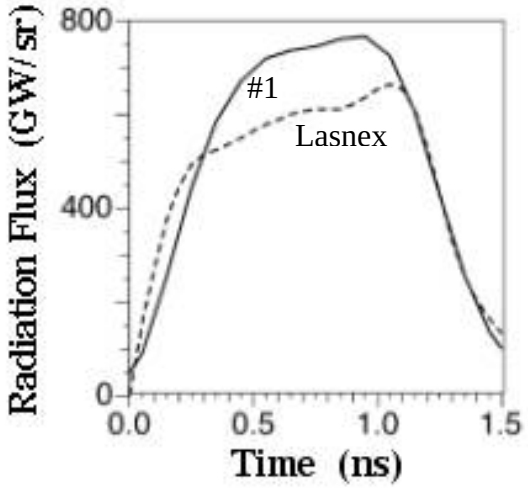


Fig. 5a

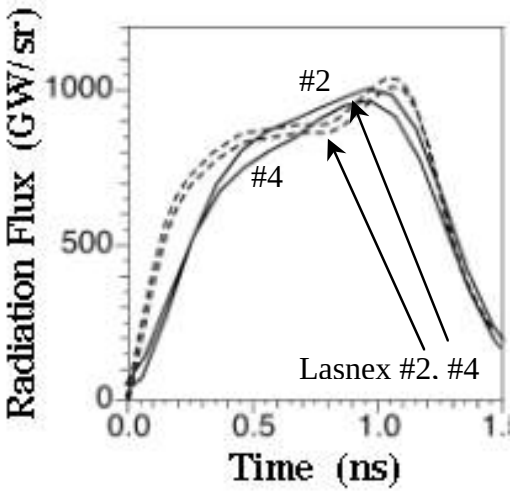


Fig. 5b

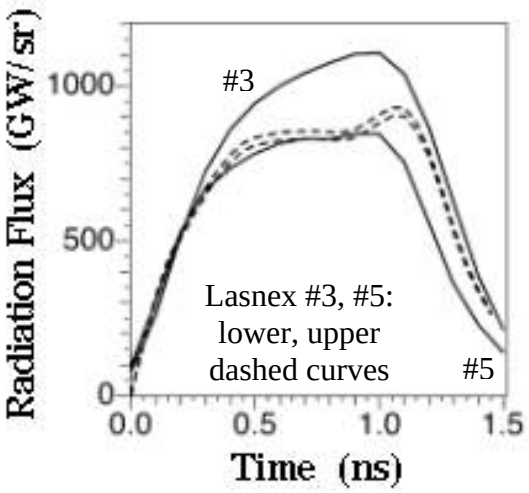
Radiation Flux (GW/sr)
1000
500
0
0.0
0.5
1.0
1.5
Time (ns)
#3
#5
Lasnex #3, #5:
lower, upper
dashed curves

Fig. 5c

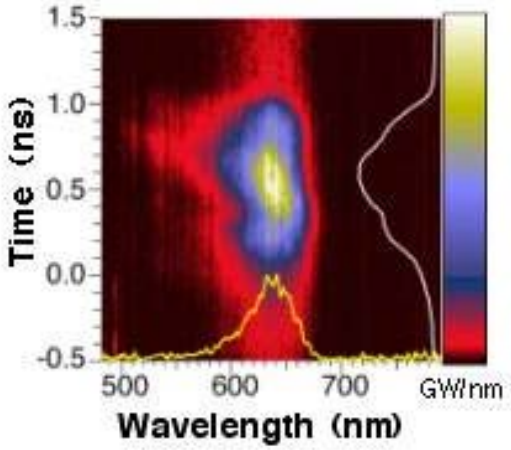


Fig. 6a

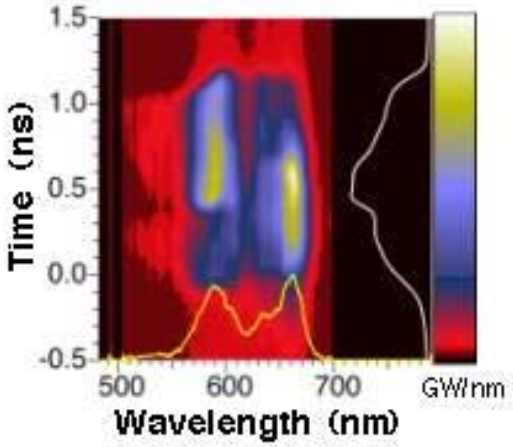


Fig. 6b

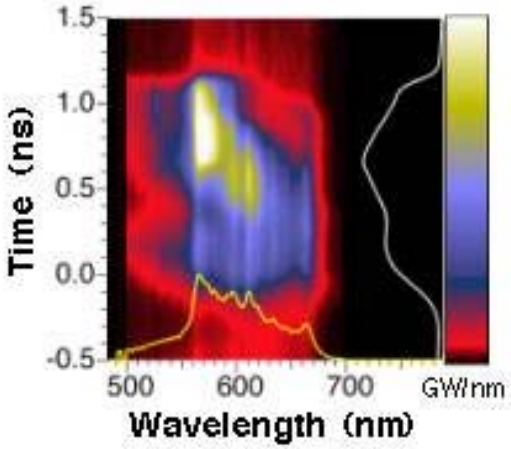


Fig. 6c

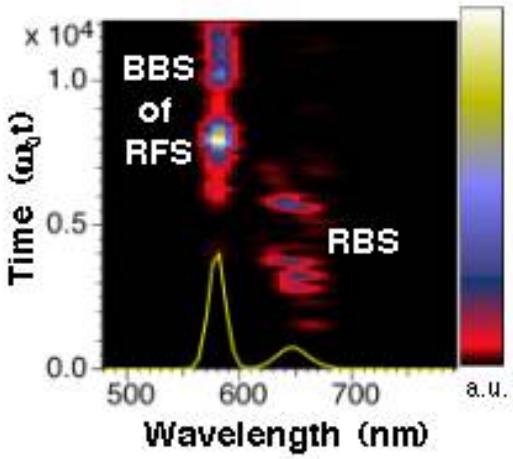
x 10^4
1.0
0.5
0.0
Time (ω0t)
BBS
of
RFS
RBS
500
600
700
Wavelength (nm)
a.u.

Fig. 6d